

# Electron Dynamics at High-Energy Densities in Nickel from Non-linear Resonant X-ray Absorption Spectra

Robin Y. Engel,<sup>1,2</sup> Oliver Alexander,<sup>3</sup> Kaan Atak,<sup>1</sup> Uwe Bovensiepen,<sup>4,5</sup> Jens Buck,<sup>1,6</sup> Robert Carley,<sup>7</sup> Michele Cascella,<sup>8</sup> Valentin Chardonnet,<sup>9</sup> Gheorghe Sorin Chiuzbaian,<sup>9</sup> Christian David,<sup>10</sup> Florian Döring,<sup>10</sup> Andrea Eschenlohr,<sup>4</sup> Natalia Gerasimova,<sup>7</sup> Frank de Groot,<sup>11</sup> Loïc Le Guyader,<sup>7</sup> Oliver S. Humphries,<sup>7</sup> Manuel Izquierdo,<sup>7</sup> Emmanuelle Jal,<sup>9</sup> Adam Kubec,<sup>10</sup> Tim Laarmann,<sup>1,12</sup> Charles-Henri Lambert,<sup>13</sup> Jan Lüning,<sup>14</sup> Jonathan P. Marangos,<sup>3</sup> Laurent Mercadier,<sup>7</sup> Giuseppe Mercurio,<sup>7</sup> Piter S. Miedema,<sup>1</sup> Katharina Ollefs,<sup>4</sup> Bastian Pfau,<sup>15</sup> Benedikt Rösner,<sup>10</sup> Kai Rossnagel,<sup>1,6</sup> Nico Rothenbach,<sup>4</sup> Andreas Scherz,<sup>7</sup> Justine Schlappa,<sup>7</sup> Markus Scholz,<sup>1,7</sup> Jan O. Schunck,<sup>1,2</sup> Kiana Setoodehnia,<sup>7</sup> Christian Stamm,<sup>13,16</sup> Simone Techert,<sup>1,17</sup> Sam M. Vinko,<sup>18,19</sup> Heiko Wende,<sup>4</sup> Alexander A. Yaroslavtsev,<sup>20</sup> Zhong Yin,<sup>21,22</sup> and Martin Beye<sup>1,2</sup>

<sup>1</sup>*Deutsches Elektronen-Synchrotron DESY, Notkestr. 85, 22607 Hamburg, Germany*

<sup>2</sup>*Department of Physics, Universität Hamburg, Luruper Chaussee 149, 22761 Hamburg, Germany*

<sup>3</sup>*Imperial College London, Department of Physics, Exhibition Rd, London SW7 2BX, United Kingdom*

<sup>4</sup>*Faculty of Physics and Center for Nanointegration Duisburg-Essen (CENIDE), University of Duisburg-Essen, Lotharstr. 1, 47057 Duisburg, Germany*

<sup>5</sup>*Institute for Solid State Physics, University of Tokyo, Kashiwa, Chiba, 277-8581, Japan*

<sup>6</sup>*Christian-Albrechts-Universität zu Kiel, Institut für Experimentelle und Angewandte Physik, Leibnizstraße 11-19, 24118 Kiel, Germany*

<sup>7</sup>*European XFEL, Holzkoppel 4, 22869 Schenefeld, Germany*

<sup>8</sup>*MAX IV Laboratory, Lund University, PO Box 118, SE-221 00 Lund, Sweden*

<sup>9</sup>*Sorbonne Université, CNRS, Laboratoire de Chimie Physique-Matière et Rayonnement, 4 Pl. Jussieu Barre 43-44, 75005 Paris, France*

<sup>10</sup>*Paul Scherrer Institut, Forschungsstrasse 111, 5232 Villigen, Switzerland*

<sup>11</sup>*Utrecht University, Debye Institute for Nanomaterials Science, Inorganic Chemistry and Catalysis, Princetonplein 1, Universiteitsweg 99, 3584 CC Utrecht, Netherlands*

<sup>12</sup>*The Hamburg Centre for Ultrafast Imaging CUI, Luruper Chaussee 149, 22761 Hamburg, Germany*

<sup>13</sup>*Department of Materials, ETH Zurich, 8093 Zurich, Switzerland*

<sup>14</sup>*Helmholtz-Zentrum Berlin für Materialien und Energie GmbH, Hahn-Meitner-Platz 1, 14109 Berlin, Germany*

<sup>15</sup>*Max Born Institute for Nonlinear Optics and Short Pulse Spectroscopy, Max-Born-Str. 2A, 12489 Berlin, Germany*

<sup>16</sup>*Institute for Electric Power Systems, University of Applied Sciences and Arts Northwestern Switzerland, 5210 Windisch, Switzerland*

<sup>17</sup>*Institute for X-ray Physics, Goettingen University, Friedrich Hund Platz 1, 37077 Goettingen, Germany*

<sup>18</sup>*Department of Physics, Clarendon Laboratory, University of Oxford, Parks Road, Oxford OX1 3PU, United Kingdom*

<sup>19</sup>*Central Laser Facility, STFC Rutherford Appleton Laboratory, Didcot OX11 0QX, United Kingdom*

<sup>20</sup>*Uppsala University, Department of Physics and Astronomy, Regementsvägen 1 Uppsala, Sweden*

<sup>21</sup>*International Center for Synchrotron Radiation Innovation Smart, Tohoku University, 2-1-1 Katahira, Aoba-ku, Sendai, Miyagi 980-8577, Japan*

<sup>22</sup>*ETH Zürich, Laboratorium für Physikalische Chemie, Vladimir-Prelog-Weg 1-5, 8093 Zürich, Switzerland*

(Dated: December 1, 2022)

The pulse intensity from X-ray free-electron lasers (FELs) can create extreme excitation densities in solids, entering the regime of non-linear X-ray-matter interactions. We show  $L_3$ -edge absorption spectra of metallic nickel thin films with fluences entering a regime where several X-ray photons are incident per absorption cross-section. Main features of the observed non-linear spectral changes are described with a predictive rate model for electron population dynamics during the pulse, utilizing a fixed density of states and tabulated ground-state properties.

The modern understanding of complex solid materials relies on appropriate approximations to the unabridged quantum mechanical description of the full, correlated many-body problem. To assess the predictive power of theoretical models and the selected approximations, detailed experimental studies far away from known territory

are especially insightful. Absorbing the high power densities available from an X-ray free-electron laser (FEL) in a solid metal generates a very unusual state of warm dense matter far from equilibrium: Individual electronic excitations reach up to hundreds of eV and excitation levels average out to many eV per atom [1–9]. As the absorp-

tion of an intense X-ray pulse depends on the changes it drives in the electronic system [10–16], a single-pulse non-linear absorption measurement can be used to investigate its evolution on the timescale of the pulse duration.

We present fluence-dependent X-ray absorption spectra recorded with monochromatic X-rays on metallic nickel thin films around the nickel  $2p_{3/2}$  ( $L_3$ ) edge, revealing a changing valence electron system around the Fermi level as a consequence of the high excitation densities from fluences up to  $60 \text{ J/cm}^2$  (corresponding to  $2 \times 10^{15} \text{ W/cm}^2$ ).

The electronic processes that ensue after the absorption of photons at core levels trigger a complex dynamical process that is challenging to treat in purely *ab-initio* simulations [17–21]. Here, we take an alternative approach and develop a simple rate equation model that provides an intuitive understanding of the relevant processes [22]. The resulting picture of the evolution of electronic populations within a fixed ground-state density of states successfully describes the largest part of the non-linear changes in the spectra. This corroborates the dominant impact of electron redistribution from the strong non-equilibrium state towards a thermalized electronic system. Some of the observed changes, especially in the close vicinity of the resonance, deviate from the predictions of the rate model and call for more evolved theories. Here, our work provides a benchmark to identify observations of advanced physical processes and effects. While this letter discusses the experiment and resulting insights, we lay out the framework of the model in detail in a separate publication [22].

Additionally, our straightforward picture of intense core-resonant X-ray pulse interaction with the valence system of a  $3d$  metal lays a solid knowledge-based foundation for the planning and interpretation of non-linear X-ray spectroscopy experiments at FELs; in particular, the relevance of electronic scattering processes observed here is expected to affect methods relying on stimulated emission from core excitations and X-ray or X-ray/optical wave-mixing [23–38].

X-ray absorption spectra of the nickel  $2p_{3/2}$  ( $L_3$ ) edge were recorded at the Spectroscopy and Coherent Scattering Instrument (SCS) of the European XFEL [40].

The XAS spectra were measured by continuously scanning the SASE3 monochromator [41] (synchronized with the undulator gap) back-and-forth many times in the range 846–856 eV. The photon bandwidth was about 420 meV and the FEL pulse duration on the sample was about 30 fs FWHM. The overall beam intensity was controlled using a gas attenuator filled with nitrogen and monitored using an X-ray gas-monitor (XGM) downstream of the monochromator [42, 43].

For X-ray absorption measurements at FELs based on Self-Amplified Spontaneous Emission (SASE), beam-splitting schemes can deliver optimal normalization of SASE-fluctuations [44–46]. Here, a focusing and beam-splitting zone plate also creates the required tight focusing to achieve extreme fluences. Figure 1 shows the

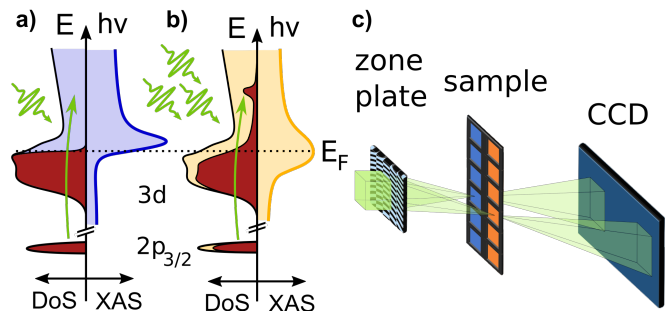


FIG. 1. (a&b) Sketch of absorption at different fluences. The unoccupied states determine the XAS spectrum as they are probed by core-resonant photons. (a) In the low-fluence case (blue unoccupied states and resulting spectrum), the electronic system mostly remains in the ground state. (b) In the high-fluence case (yellow unoccupied states and spectrum), later parts of the X-ray pulse probe a hot electronic system and experience spectral bleaching at the probed photon energy.

**Setup for non-linear XAS** (c) The split-beam-normalization scheme uses a special zone plate [39], which generates two adjacent beam foci for transmission through the sample and a reference membrane before the beams impinge on the detector.

schematic experimental layout.

The zone plate combines an off-axis Fresnel structure for focusing and a line grating for beam-splitting in a single optical element [39]. It thus produces two  $\mu\text{m}$ -sized, identical foci in the sample plane, 1.9 mm apart, originating from the first-order diffraction of the zone plate, as well as the positive and negative first orders of the line grating. The sample has a square support of 25 mm size, containing  $\text{Si}_3\text{N}_4$  membrane windows (orange in Figure 1) of 0.5 mm size and 200 nm thickness with a distance of 2 mm between adjacent windows. Every second pair of rows (blue in Figure 1) was additionally coated with a 20 nm sample layer of polycrystalline metallic Ni by sputter deposition, on top of a 2 nm bonding layer of Ta; a 2 nm Pt capping layer prevents oxidation during sample-handling.

The sample frame was positioned such that one zone plate focus impinged on a nickel-coated membrane, while the other hit a bare silicon-nitride membrane. Thus, the difference in transmission of both beams can be attributed solely to the nickel film.

The detector was a fast readout-speed charge-coupled device (FastCCD) with high dynamic range, enabling 10 Hz read-out and increasing the fluence range available to the experiment [47–49]. Due to the unstable detector temperature, significant retroactive calibration of the detector was necessary (see supplement). To prevent detector saturation, an additional aluminum filter of about  $13 \mu\text{m}$  thickness was used between sample and detector for measurements with the unattenuated beam.

During these high-intensity measurements, sample and reference films were locally damaged by intense individ-

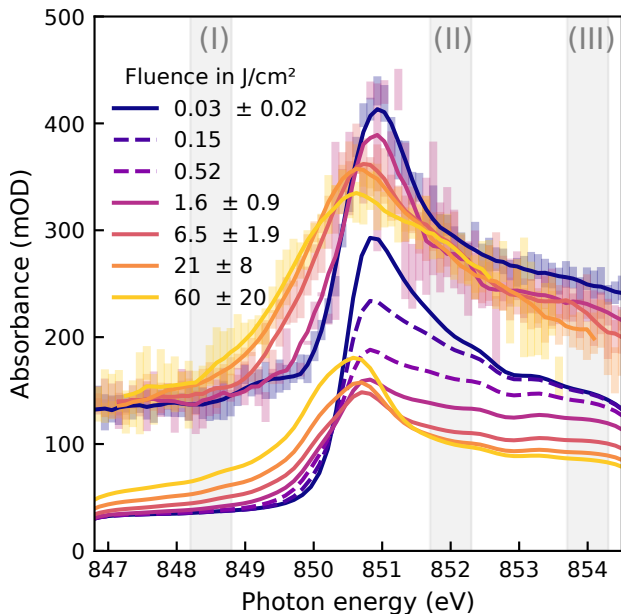


FIG. 2. **Fluence-dependent Ni  $L_3$ -edge spectra, measured (top) and simulated (bottom).** The fluence of events contributing to each spectrum is given in the legend in terms of mean and standard deviation. Dashed simulated spectra do not have a corresponding measurement. The regions of interest from which absorbance changes shown in panels b), d), and e) of Figure 3 were quantified are shaded and labeled (I), (II), and (III), respectively. The error bars are shown for the measured spectra and represent the 95% confidence intervals for each bin of 102 meV width; solid lines of the measured spectra are smoothed using a Savitzky-Golay filter using windows of 21 bins and 4th-order polynomials. The experimental spectra are vertically offset by 100 mOD.

ual FEL shots. Thus, the FEL was operated in single-shot mode at 10 Hz repetition rate, and the sample was scanned through the beam continuously at  $0.5 \text{ mm} \cdot \text{s}^{-1}$ , resulting in 10 shots per membrane window.

The shot craters in the reference membranes were later analyzed with scanning electron microscopy (SEM) to determine the effective focal size at specific photon energies. The resulting spot sizes were used to calibrate ray-tracing calculations which delivered the photon-energy-dependent spot size, ranging from  $0.4 \mu\text{m}^2$  to about  $3 \mu\text{m}^2$  (see supplement for details on the spot size determination).

Figure 2 shows the spectra for the nickel  $L_3$ -edge next to simulated spectra for increasing X-ray fluence over more than 3 orders or magnitude, from  $0.03$  to  $60 \text{ J/cm}^2$ . Each measured point represents an average of several FEL shots, sorted by X-ray fluence and photon energy. The varying statistical uncertainty is a result of the pulse intensity fluctuations of monochromatized SASE radiation [50] in combination with photon energy-dependent spot sizes (see supplement for details on the shot sorting).

We observe four main fluence-dependent effects, which we quantify and compare to the simulated results in Fig-

ure 3: a) a red-shift of the absorption peak of up to  $0.9 \pm 0.1 \text{ eV}$  in the rising flank; b) an increase of the pre-edge absorbance, as the rising edge of the absorption peak shifts and broadens; c) a reduced peak absorbance and d), e) a reduced post-edge absorbance. The integration regions from which the effects b), d) and e) are derived, are highlighted in Figure 2 as (I), (II) and (III), respectively. The shift of the absorption edge is quantified by the photon energy at which the absorbance reaches half of the peak value; its uncertainty is propagated from the statistical uncertainty of the absorption peak measurement.

Before we analyze these observations in detail, let us quickly paraphrase our modeling approach [22]: In contrast to earlier rate models [12, 51], we describe the evolution of the electronic system with an energy-resolved population of the valence band. Tracking the full non-thermal population history proved crucial to describe the non-linear absorption changes near and around the Fermi level. As coupling between electrons and phonons in metals is typically not yet important on the timescale of 30 fs [52–54] and we do not account for collective electron correlation effects, we test the approximation that the Density of States (DoS) remains unchanged within the pulse duration.

Transition rates between electronic states are determined by scaling ground state rates with the populations of initial and final states. The relevant process rates are compiled into differentials of electronic populations and photon density in space and time and implemented in a finite-element simulation to derive the electron population history and ultimately the X-ray transmission of a three-dimensional sample.

The model implements the processes of resonant absorption from the  $2p_{3/2}$  core level and non-resonant absorption from other (mostly valence) electrons. Stimulated emission is described as a time-inverted resonant absorption process. Electronic thermalization is modeled with a bulk timescale  $\tau_{\text{th}}$  (essentially quantifying electron-electron scattering) that moves the non-thermal valence electron distribution towards a target Fermi-Dirac distribution that corresponds to the momentary internal energy and population of the valence band. Finally, scattering cascades initiated by fast Auger-electrons and photo-electrons from non-resonant absorption are parameterized by another scattering time  $\tau_{\text{scatt}}$ .

With this simple description of the underlying processes, we provide a microscopic picture of the electronic system and its interaction with resonant X-rays as a complementary approach to more complex calculations [20, 21].

Solely considering the population dynamics of the electronic system, the simulation already achieves good agreement with the experimental data across more than three orders of magnitude in fluence. This is particularly remarkable since nearly all input parameters are experimental parameters or well-known ground-state properties

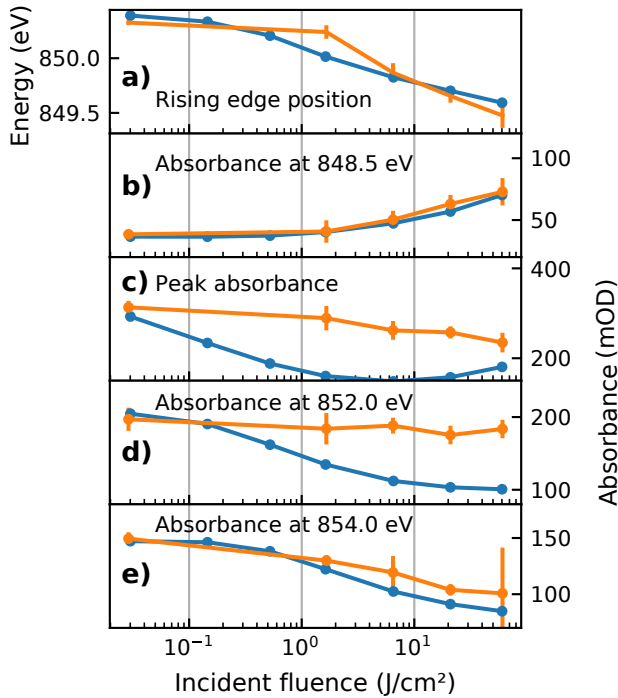


FIG. 3. **Comparison of spectral effects** between simulation (blue lines) and experiment (orange lines with error bars). The shift of absorption edge in panel a) represents the photon energy at which the half-maximum of the absorption peak is reached. The absorbance changes in panels b), d) and e) are integrated from the gray shaded regions in Figure 2, while panel c) shows the global maximum of the spectrum.

of the material, such as density, electronic configuration, and ground-state spectrum. Only the valence thermalization time  $\tau_{th}$  and electron scattering time  $\tau_{scatt}$  were varied to achieve the best match to the experimental results. The found value  $\tau_{th} = 6$  fs compares well to recent estimates for excitations on this energy scale [33, 38, 55, 56].

The time constant  $\tau_{scatt} = 1.5$  fs characterizes the secondary electron scattering cascade which transfers energy (and population) from fast electrons to (unoccupied) valence states. The constant summarizes many individual electron scattering events and compares to the tabulated time between individual collisions in ground-state nickel of roughly 100 attoseconds [57].

Figure 4 shows an example of a simulated valence band population history, specifically from the uppermost 4 Å thick layer of the sample, excited with a Gaussian pulse profile centered around  $t = 0$  with 30 fs FWHM duration and  $30 \text{ J/cm}^2$  fluence. While panel a) shows the calculated DoS as used by the simulation and published in [58, 59], the colormap in b) shows the occupation of these states over time. Panel c) shows the number of electrons per atom in the valence band below and above the Fermi level (blue solid and dashed curves, respectively) as well as the average number of core holes and the number of free electrons over time. Even though the direct interaction with the photons creates core holes via

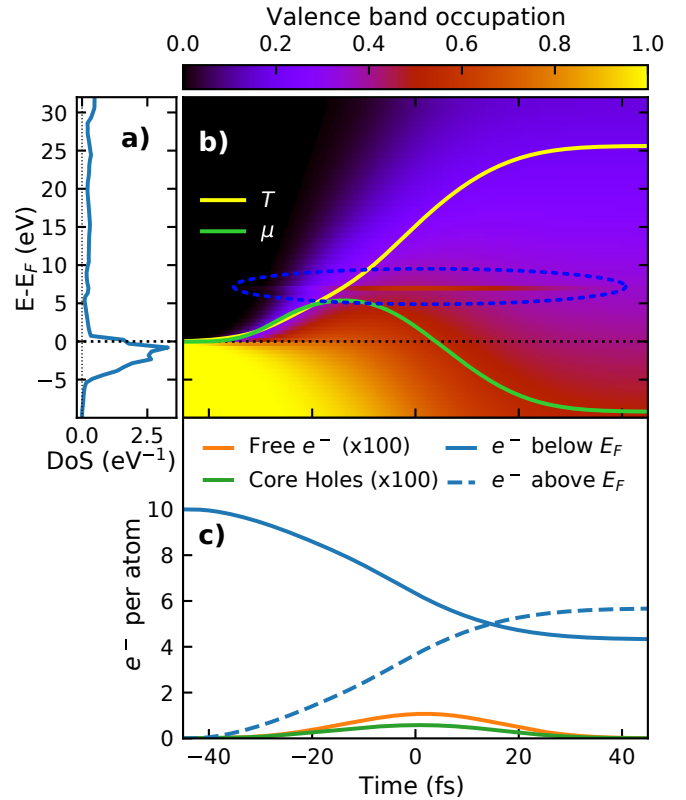


FIG. 4. **Evolution of electronic populations (simulation)** in a single voxel at the sample surface for a pulse of  $858.3 \text{ eV}$ , with a pulse energy of  $30 \text{ J/cm}^2$ . Panel a) shows the total DoS used as an input for the simulation. Panel b) shows the energy-resolved (relative to the Fermi energy) occupation of the valence band over time. The population (in electrons/atom/eV) is the product of the DoS and the occupation. The thermalized valence occupation lags a few femtoseconds behind the current chemical potential  $\mu$ ; the temperature  $T$  of the valence system rises rapidly, ultimately reaching up to  $25 \text{ eV}$ . The bleaching of valence states (highlighted with a blue dotted ellipse) is visible as a high non-thermal population at the resonant photon energy around  $7 \text{ eV}$  above the Fermi level. Panel c) shows the number of core holes and free electrons over time, as well as the number of electrons in the valence system below and above the Fermi energy.

resonant absorption and free electrons via non-resonant absorption, the excitation energy of both processes is so quickly transferred to the valence electrons that only the valence electron distribution ever deviates strongly from the ground state. By the end of the pulse in this example, more than half of the  $3d$  valence electrons are excited to valence states above the Fermi level, while the highest instantaneous number of core holes was only about one per 100 atoms, as shown in Figure 4 c). Due to the small-bandwidth excitation, the core- and resonant valence states operate like a two-level system. Since the number of resonant valence states is small in comparison to the number of core electrons, the resonant absorption process saturates due to occupied valence states long be-

fore the core level is depleted. A heated Fermi-Dirac distribution further contributes to the occupation of states above the Fermi level.

Since in our experiment, the same monochromatic pulse excites and probes the sample, the situation is different for energies below the edge: absorption only rises after non-resonant absorption has led to sufficient electronic heating until the tail of the hot hole distribution reaches the probed energy. Only then, additional resonant absorption begins to occur and accelerates further electronic heating and in turn additional pre-edge absorption. Since this process occurs exponentially faster near the absorption edge, it contributes significantly to the observed spectral red-shift (see Figure 3 a) and b)).

Another cause of the observed edge shift is the shift of the chemical potential  $\mu$ , which strongly depends on the exact shape of the DoS and is shown in Figure 4 b) as a green line. Initially,  $\mu$  increases with absorbed fluence, as thermally excited electrons from the  $3d$  states must spread out in energy to the lower DoS above the Fermi level. With rising electronic temperature, the high DoS of the  $3d$  states becomes less relevant and the chemical potential drops again as expected in regular metals. A similar evolution of the chemical potential and electronic temperature was predicted for optically excited nickel by previous experiments and calculations [4, 60–62].

A significant deviation between model and experiment can be observed at the resonance peak itself, where the simulated electron dynamics lead us to expect a much stronger saturation effect than observed experimentally (Figure 3 c)). This underestimation may be related to a fluence-dependent decrease of the excited state lifetime and consequent energetic broadening of the resonant core-valence transition, which is not considered in our model. While it is unsurprising to find additional resonant effects in the resonance peak itself, the lack of any significant saturation around 852 eV (Figure 3 d)) is even more surprising. Both disagreements point to additional physical effects and call for more sophisticated models.

We speculatively propose mechanisms which could contribute to these disagreements: The transition matrix elements could get modified at higher excitation densities, especially around the resonance, while we model the absorption only based on the ground-state spectrum. An energy dependence of the electron-electron scattering cross-section could allow for particularly fast scattering of electrons with certain energies, counteracting the saturation. Furthermore, a collective, correlated response of the electronic system could modify the DoS or the transitions even on the fast time scale of the FEL pulse duration [63]. Despite these remaining discrepancies, the main aspects of the spectral changes are covered in our very simple population dynamics model.

We want to point out that substantially smaller spectral red-shifts were observed before in nickel after excitation with optical lasers, albeit at three orders of magnitude lower excitation fluence. These required qualita-

tively different interpretations [56, 63–65], where the explanation for time-dependent changes included a variable DoS, calculated using (Time-Dependent) Density Functional Theory (TD)DFT; this dependency is overshadowed in our high-fluence study by the effects of electron population dynamics.

To summarize, we interpret the fluence-dependent near-edge X-ray absorption spectra of the nickel  $2p_{3/2}$  core level at X-ray fluences of up to  $60 \text{ J/cm}^2$ . We propose a rate-equation model, describing the various excitation and decay processes that connect core- and valence electronic states using differential equations based on scaling of known ground-state properties with the evolving electron populations. For the measured spectra of metallic nickel, the model successfully predicts the increase of absorption before and its decrease beyond the resonance, as well as the observed shift of the absorption peak over more than three orders of magnitude in fluence.

It therefore allows us to identify the most important processes responsible for spectral changes: Heating of valence electrons due to secondary electron cascades from Auger electrons, as well as electrons emitted from the valence band due to non-resonant absorption, appeared particularly relevant. Furthermore, saturation appears dominated to by the heated valence states rather than the core holes.

This study provides the fingerprints of how strong X-ray fluences may alter the electronic system and thus the spectra in studies, where the X-ray pulses were originally assumed to be non-disturbing. It becomes clear that a complete modeling of high-fluence spectra needs to build upon dominant population dynamics and requires special treatment around resonances. This provides an excellent benchmark for sophisticated theories. Our results also apply to the resonant regime which is particularly interesting for pioneering non-linear X-ray studies.

## ACKNOWLEDGMENTS

We acknowledge European XFEL in Schenefeld, Germany, for provision of X-ray free-electron laser beamtime at the SCS instrument and would like to thank the staff for their assistance. Funding by the Deutsche Forschungsgemeinschaft (DFG, German Research Foundation) - Project-ID 278162697 - SFB 1242 and the Helmholtz Association (grant VH-NG-1105) is gratefully acknowledged. Access to Synchrotron SOLEIL through proposal ID 20160880 for characterization of static properties of the Ni films is acknowledged. Parts of this work were funded by the Swiss National Science Foundation (Grants No. PZ00P2-179944)



## AUTHOR CONTRIBUTIONS

M.B., C.D., F.D., L.L.G., J.L., J.P.M., B.R. and S.T. conceptualized and planned the experiment; M.C., C.D., F.D., N.G., L.L.G., M.I., E.J., A.K., C.-H.L., L.M., B.P., B.R., A.S., K.S., C.S., H.W. and A.Y. prepared the measurement apparatus and samples; O.A., K.A., M.B., J.B., R.C., M.C., V.C., G.S.C., C.D., F.D., R.Y.E., A.E., N.G., L.L.G., O.S.H., M.I., L.M., G.M., P.S.M., B.R.,

N.R., A.S., J.S., S.T. A.Y. and Z.Y. performed the experiment; O.A., R.Y.E., L.L.G., O.S.H., B.R. and N.R. analyzed and visualized the results; M.B. and R.Y.E. wrote the manuscript; M.B., U.B., C.D., R.Y.E., A.E., L.L.G., O.S.H., M.I., E.J., T.L., P.S.M., K.O., K.R., M.S., J.O.S., S.M.V., H.W. and Z.Y. reviewed and edited the manuscript; M.B. and J.P.M. supervised or administered the project.

- 
- [1] U. Zastra, C. Fortmann, R. R. Fäustlin, L. F. Cao, T. Döppner, S. Düsterer, S. H. Glenzer, G. Gregori, T. Laarmann, H. J. Lee, A. Przystawik, P. Radcliffe, H. Reinholz, G. Röpke, R. Thiele, J. Tiggesbäumker, N. X. Truong, S. Toleikis, I. Uschmann, A. Wierling, T. Tschentscher, E. Förster, and R. Redmer, Bremsstrahlung and line spectroscopy of warm dense aluminum plasma heated by xuv free-electron-laser radiation, *Phys. Rev. E* **78**, 066406 (2008).
- [2] S. M. Vinko, O. Ciricosta, B. I. Cho, K. Engelhorn, H.-K. Chung, C. R. D. Brown, T. Burian, J. Chalupský, R. W. Falcone, C. Graves, V. Hájková, A. Higginbotham, L. Juha, J. Krzywinski, H. J. Lee, M. Messerschmidt, C. D. Murphy, Y. Ping, A. Scherz, W. Schlotter, S. Toleikis, J. J. Turner, L. Vysin, T. Wang, B. Wu, U. Zastra, D. Zhu, R. W. Lee, P. A. Heimann, B. Nagler, and J. S. Wark, Creation and diagnosis of a solid-density plasma with an X-ray free-electron laser, *Nature* **482**, 59 (2012).
- [3] B. I. Cho, K. Engelhorn, S. M. Vinko, H.-K. Chung, O. Ciricosta, D. S. Rackstraw, R. W. Falcone, C. R. D. Brown, T. Burian, J. Chalupský, C. Graves, V. Hájková, A. Higginbotham, L. Juha, J. Krzywinski, H. J. Lee, M. Messerschmidt, C. Murphy, Y. Ping, N. Rohringer, A. Scherz, W. Schlotter, S. Toleikis, J. J. Turner, L. Vysin, T. Wang, B. Wu, U. Zastra, D. Zhu, R. W. Lee, B. Nagler, J. S. Wark, and P. A. Heimann, Resonant  $K\alpha$  Spectroscopy of Solid-Density Aluminum Plasmas, *Physical Review Letters* **109**, 245003 (2012).
- [4] O. S. Humphries, R. S. Marjoribanks, Q. Y. van den Berg, E. C. Galtier, M. F. Kasim, H. J. Lee, A. J. F. Mescampbell, B. Nagler, R. Royle, J. S. Wark, and S. M. Vinko, Probing the electronic structure of warm dense nickel via resonant inelastic x-ray scattering, *Phys. Rev. Lett.* **125**, 195001 (2020).
- [5] E. García Saiz, G. Gregori, D. O. Gericke, J. Vorberger, B. Barbrel, R. J. Clarke, R. R. Freeman, S. H. Glenzer, F. Y. Khattak, M. Koenig, O. L. Landen, D. Neely, P. Neumayer, M. M. Notley, A. Pelka, D. Price, M. Roth, M. Schollmeier, C. Spindloe, R. L. Weber, L. Van Wierkom, K. Wünsch, and D. Riley, Probing warm dense lithium by inelastic X-ray scattering, *Nature Physics* **4**, 940 (2008).
- [6] S. M. Vinko, X-ray free-electron laser studies of dense plasmas, *Journal of Plasma Physics* **81**, 365810501 (2015).
- [7] J. E. Bailey, T. Nagayama, G. P. Loisel, G. A. Rochau, C. Blancard, J. Colgan, P. Cosse, G. Faussurier, C. J. Fontes, F. Gilleron, I. Golovkin, S. B. Hansen, C. A. Iglesias, D. P. Kilcrease, J. J. MacFarlane, R. C. Mancini, S. N. Nahar, C. Orban, J. C. Pain, A. K. Pradhan, M. Sherrill, and B. G. Wilson, A higher-than-predicted measurement of iron opacity at solar interior temperatures, *Nature* **517**, 56 (2015).
- [8] P. Hollebon, O. Ciricosta, M. P. Desjarlais, C. Cacho, C. Spindloe, E. Springate, I. C. E. Turcu, J. S. Wark, and S. M. Vinko, Ab initio simulations and measurements of the free-free opacity in aluminum, *Physical Review E* **100**, 043207 (2019), arXiv:1806.02726.
- [9] T. R. Preston, S. M. Vinko, O. Ciricosta, P. Hollebon, H.-K. Chung, G. L. Dakovski, J. Krzywinski, M. Minitti, T. Burian, J. Chalupský, V. Hájková, L. Juha, V. Vozda, U. Zastra, R. W. Lee, and J. S. Wark, Measurements of the K-Shell Opacity of a Solid-Density Magnesium Plasma Heated by an X-Ray Free-Electron Laser, *Physical Review Letters* **119**, 085001 (2017).
- [10] B. Nagler, U. Zastra, R. R. Fäustlin, S. M. Vinko, T. Whitcher, A. J. Nelson, R. Sobierajski, J. Krzywinski, J. Chalupsky, E. Abreu, S. Bajt, T. Bornath, T. Burian, H. Chapman, J. Cihelka, T. Döppner, S. Düsterer, T. Dzelzainis, M. Fajardo, E. Förster, C. Fortmann, E. Galtier, S. H. Glenzer, S. Göde, G. Gregori, V. Hájková, P. Heimann, L. Juha, M. Jurek, F. Y. Khattak, A. R. Khorsand, D. Klinger, M. Kozlova, T. Laarmann, H. J. Lee, R. W. Lee, K.-H. Meiwes-Broer, P. Mercere, W. J. Murphy, A. Przystawik, R. Redmer, H. Reinholz, D. Riley, G. Röpke, F. Rosmej, K. Saksl, R. Schott, R. Thiele, J. Tiggesbäumker, S. Toleikis, T. Tschentscher, I. Uschmann, H. J. Vollmer, and J. S. Wark, Turning solid aluminium transparent by intense soft x-ray photoionization, *Nature Physics* **5**, 693 (2009).
- [11] V. Recoules and S. Mazevet, Temperature and density dependence of XANES spectra in warm dense aluminum plasmas, *Physical Review B* **80**, 064110 (2009).
- [12] A. Di Cicco, K. Hatada, E. Giangrisostomi, R. Gunnella, F. Bencivenga, E. Principi, C. Masciovecchio, and A. Filippini, Interplay of electron heating and saturable absorption in ultrafast extreme ultraviolet transmission of condensed matter, *Phys. Rev. B* **90**, 220303(R) (2014).
- [13] D. S. Rackstraw, O. Ciricosta, S. M. Vinko, B. Barbrel, T. Burian, J. Chalupský, B. I. Cho, H.-K. Chung, G. L. Dakovski, K. Engelhorn, V. Hájková, P. Heimann, M. Holmes, L. Juha, J. Krzywinski, R. W. Lee, S. Toleikis, J. J. Turner, U. Zastra, and J. S. Wark, Saturable absorption of an x-ray free-electron-laser heated solid-density aluminum plasma, *Phys. Rev. Lett.* **114**, 015003 (2015).
- [14] E. Principi, E. Giangrisostomi, R. Cucini, F. Bencivenga,

- A. Battistoni, A. Gessini, R. Mincigrucci, M. Saito, S. Di Fonzo, F. D'Amico, A. Di Cicco, R. Gunnella, A. Filipponi, A. Giglia, S. Nannarone, and C. Masciovecchio, Free electron laser-driven ultrafast rearrangement of the electronic structure in Ti, *Structural Dynamics* **3**, 023604 (2016).
- [15] Z. Chen, D. J. Higley, M. Beye, M. Hantschmann, V. Mehta, O. Hellwig, A. Mitra, S. Bonetti, M. Bucher, S. Carron, T. Chase, E. Jal, R. Kukreja, T. Liu, A. H. Reid, G. L. Dakovski, A. Föhlisch, W. F. Schlotter, H. A. Dürr, and J. Stöhr, Ultrafast Self-Induced X-Ray Transparency and Loss of Magnetic Diffraction, *Physical Review Letters* **121**, 137403 (2018).
- [16] H. Yoneda, Y. Inubushi, M. Yabashi, T. Katayama, T. Ishikawa, H. Ohashi, H. Yumoto, K. Yamauchi, H. Mimura, and H. Kitamura, Saturable absorption of intense hard x-rays in iron, *Nature communications* **5**, 5080 (2014).
- [17] M. Chen and K. Lopata, First-Principles Simulations of X-ray Transient Absorption for Probing Attosecond Electron Dynamics, *Journal of Chemical Theory and Computation* **16**, 4470 (2020).
- [18] C. Mo, Z.-G. Fu, P. Zhang, W. Kang, W. Zhang, and X. T. He, First-principles method for x-ray Thomson scattering including both elastic and inelastic features in warm dense matter, *Physical Review B* **102**, 195127 (2020).
- [19] G. O. Williams and M. Fajardo, Collisional ionization and recombination in degenerate plasmas beyond the free-electron-gas approximation, *Phys. Rev. E* **102**, 063204 (2020).
- [20] N. Medvedev, V. Tkachenko, V. Lipp, Z. Li, and B. Ziaja, Various damage mechanisms in carbon and silicon materials under femtosecond x-ray irradiation, *4open* **1**, 3 (2018).
- [21] V. Lipp, V. Tkachenko, M. Stransky, B. Aradi, T. Frauenheim, and B. Ziaja, Density functional tight binding approach utilized to study x-ray-induced transitions in solid materials, *Scientific reports* **12**, 1551 (2022).
- [22] R. Y. Engel, M. Scholz, J. O. Schunck, and M. Beye, A rate-model for nonlinear x-ray near edge absorption spectra, Jointly submitted to Phys. Rev. B (2022).
- [23] S. Mukamel, Multiple core-hole coherence in x-ray four-wave-mixing spectroscopies, *Phys. Rev. B* **72**, 235110 (2005).
- [24] T. E. Glover, D. M. Fritz, M. Cammarata, T. K. Allison, S. Coh, J. M. Feldkamp, H. Lemke, D. Zhu, Y. Feng, R. N. Coffee, M. Fuchs, S. Ghimire, J. Chen, S. Schwartz, D. A. Reis, S. E. Harris, and J. B. Hastings, X-ray and optical wave mixing, *Nature* **488**, 603 (2012).
- [25] M. Beye, S. Schreck, F. Sorgenfrei, C. Trabant, N. Pontius, C. Schüßler-Langeheine, W. Wurth, and A. Föhlisch, Stimulated x-ray emission for materials science, *Nature* **501**, 191 (2013).
- [26] C. Weninger, M. Purvis, D. Ryan, R. A. London, J. D. Bozek, C. Bostedt, A. Graf, G. Brown, J. J. Rocca, and N. Rohringer, Stimulated electronic x-ray raman scattering, *Phys. Rev. Lett.* **111**, 233902 (2013).
- [27] S. Schwartz, M. Fuchs, J. B. Hastings, Y. Inubushi, T. Ishikawa, T. Katayama, D. A. Reis, T. Sato, K. Tono, M. Yabashi, S. Yudovich, and S. E. Harris, X-ray second harmonic generation, *Physical Review Letters* **112**, 163901 (2014).
- [28] K. Tamasaku, E. Shigemasa, Y. Inubushi, T. Katayama, K. Sawada, H. Yumoto, H. Ohashi, H. Mimura, M. Yabashi, K. Yamauchi, and T. Ishikawa, X-ray two-photon absorption competing against single and sequential multiphoton processes, *Nature Photonics* **8**, 313 (2014).
- [29] F. Bencivenga, R. Cucini, F. Capotondi, A. Battistoni, R. Mincigrucci, E. Giangristostomi, A. Gessini, M. Manfreda, I. P. Nikolov, E. Pedersoli, E. Principi, C. Svetina, P. Parris, F. Casolari, M. B. Danailov, M. Kiskinova, and C. Masciovecchio, Four-wave mixing experiments with extreme ultraviolet transient gratings, *Nature* **520**, 205 (2015).
- [30] S. Schreck, M. Beye, and A. Föhlisch, Implications of stimulated resonant x-ray scattering for spectroscopy, imaging, and diffraction in the regime from soft to hard x-rays, *Journal of Modern Optics* **62**, S34 (2015).
- [31] R. K. Lam, S. L. Raj, T. A. Pascal, C. D. Pemmaraju, L. Foglia, A. Simoncig, N. Fabris, P. Miotti, C. J. Hull, A. M. Rizzuto, J. W. Smith, R. Mincigrucci, C. Masciovecchio, A. Gessini, E. Allaria, G. De Ninno, B. Diviacco, E. Roussel, S. Spampinati, G. Penco, S. Di Mitri, M. Trovò, M. Danailov, S. T. Christensen, D. Sokaras, T. C. Weng, M. Coreno, L. Poletto, W. S. Drisdell, D. Prendergast, L. Giannessi, E. Principi, D. Nordlund, R. J. Saykally, and C. P. Schwartz, Soft x-ray second harmonic generation as an interfacial probe, *Physical Review Letters* **120**, 023901 (2018).
- [32] K. Tamasaku, E. Shigemasa, Y. Inubushi, I. Inoue, T. Osaka, T. Katayama, M. Yabashi, A. Koide, T. Yokoyama, and T. Ishikawa, Nonlinear spectroscopy with x-ray two-photon absorption in metallic copper, *Physical Review Letters* **121**, 083901 (2018).
- [33] D. J. Higley, A. H. Reid, Z. Chen, A. A. L. Loïc Le Guyader and, T. Liu, T. Chase, G. L. Dakovski, A. Mitra, E. Yuan, H. A. Dürr, W. F. Schlotter, and J. Stöhr, Femtosecond x-ray induced changes of the electronic and magnetic response of solids from electron redistribution, *Nature communications* **10**, 5289 (2019).
- [34] H. Rottke, R. Y. Engel, D. Schick, J. O. Schunck, P. S. Miedema, M. C. Borchert, M. Kuhlmann, N. Ekanayake, S. Dziarzhytski, G. Brenner, U. Eichmann, C. von Korff Schmising, M. Beye, and S. Eisebitt, Probing electron and hole colocalization by resonant four-wave mixing spectroscopy in the extreme ultraviolet, *Science Advances* **8**, eabn5127 (2022).
- [35] J. R. Rouxel, D. Fainozzi, R. Mankowsky, B. Rösner, G. Seniutinas, R. Mincigrucci, S. Catalini, L. Foglia, R. Cucini, F. Döring, A. Kubec, F. Koch, F. Bencivenga, A. A. Haddad, A. Gessini, A. A. Maznev, C. Cirelli, S. Gerber, B. Pedrini, G. F. Mancini, E. Razzoli, M. Burian, H. Ueda, G. Pamfilidis, E. Ferrari, Y. Deng, A. Mozzanica, P. J. M. Johnson, D. Ozerov, M. G. Izzo, C. Bottari, C. Arrell, E. J. Divall, S. Zerdane, M. Sander, G. Knopp, P. Beaud, H. T. Lemke, C. J. Milne, C. David, R. Torre, M. Chergui, K. A. Nelson, C. Masciovecchio, U. Staub, L. Patthey, and C. Svetina, Hard X-ray transient grating spectroscopy on bismuth germanate, *Nature Photonics* **15**, 499 (2021).
- [36] F. Bencivenga, R. Mincigrucci, F. Capotondi, A. Calvi, R. Cucini, L. Foglia, E. Pedersoli, E. Principi, A. Simoncig, P. Cinquegrana, M. B. Danailov, G. De Ninno, S. Di Mitri, G. Gaio, A. Gessini, L. Giannessi, N. Mahne, M. Manfreda, I. P. Nikolov, G. M. Penco, L. Raimondi, P. R. Ribic, C. Svetina, M. Trovo, M. Zangrando, and

- C. Masciovecchio, An approach for realizing four-wave-mixing experiments stimulated by two-color extreme ultraviolet pulses, in *International Conference on X-Ray Lasers 2020*, July 2021, edited by D. Bleiner (SPIE, 2021) p. 28.
- [37] S. Wirok-Stoletow, R. Jin, D. Kolbasova, S.-K. Son, A. Aquila, and R. Santra, Nonsequential two-photon absorption in solid Ge irradiated by an intense x-ray free-electron-laser pulse, *Physical Review A* **106**, 023118 (2022).
- [38] D. J. Higley, Z. Chen, M. Beye, M. Hantschmann, A. H. Reid, V. Mehta, O. Hellwig, G. L. Dakovski, A. Mitra, R. Y. Engel, T. Maxwell, Y. Ding, S. Bonetti, M. Bucher, S. Carron, T. Chase, E. Jal, R. Kukreja, T. Liu, A. Föhlisch, H. A. Dürr, W. F. Schlotter, and J. Stöhr, Stimulated resonant inelastic x-ray scattering in a solid, *Communications Physics* **5**, 1 (2022).
- [39] F. Döring, B. Rösner, M. Langer, A. Kubec, A. Kleibert, J. Raabe, C. A. F. Vaz, M. Lebugle, and C. David, Multifocus off-axis zone plates for x-ray free-electron laser experiments, *Optica* **7**, 1007 (2020).
- [40] T. Tschentscher, C. Bressler, J. Grünert, A. Madsen, A. Mancuso, M. Meyer, A. Scherz, H. Sinn, and U. Zastrau, Photon Beam Transport and Scientific Instruments at the European XFEL, *Applied Sciences* **7**, 592 (2017).
- [41] N. Gerasimova, D. La Civita, L. Samoylova, M. Vannoni, R. Villanueva, D. Hickin, R. Carley, R. Gort, B. E. Van Kuiken, P. Miedema, L. Le Guyader, L. Mercadier, G. Mercurio, J. Schlappa, M. Teichman, A. Yaroslavtsev, H. Sinn, and A. Scherz, The soft X-ray monochromator at the SASE3 beamline of the European XFEL: from design to operation, *Journal of Synchrotron Radiation* **29**, 1299 (2022).
- [42] J. Grünert, M. P. Carbonell, F. Dietrich, T. Falk, W. Freund, A. Koch, N. Kujala, J. Laksman, J. Liu, T. Maltezopoulos, K. Tiedtke, U. F. Jastrow, A. Sorokin, E. Syresin, A. Grebentsov, and O. Brovko, X-ray photon diagnostics at the European XFEL, *Journal of Synchrotron Radiation* **26**, 1422 (2019).
- [43] T. Maltezopoulos, F. Dietrich, W. Freund, U. F. Jastrow, A. Koch, J. Laksman, J. Liu, M. Planas, A. A. Sorokin, K. Tiedtke, and J. Grünert, Operation of X-ray gas monitors at the European XFEL, *Journal of Synchrotron Radiation* **26**, 1045 (2019).
- [44] R. Y. Engel, M. Ekimova, P. S. Miedema, C. Kleine, J. Ludwig, M. Ochmann, B. Grimm-Lebsanft, R. Ma, M. Teubner, S. Dziarzhyski, G. Brenner, M. K. Czwalińska, B. Rösner, T. K. Kim, C. David, S. Herres-Pawlis, M. Rübhausen, E. T. J. Nibbering, N. Huse, and M. Beye, Shot noise limited soft x-ray absorption spectroscopy in solution at a SASE-FEL using a transmission grating beam splitter, *Structural Dynamics* **8**, 014303 (2021).
- [45] W. F. Schlotter, M. Beye, S. Zohar, G. Coslovich, G. L. Dakovski, M. F. Lin, Y. Liu, A. Reid, S. Stubbs, P. Walter, K. Nakahara, P. Hart, P. S. Miedema, L. Le Guyader, K. Hofhuis, P. T. P. Le, J. E. T. Elshof, H. Hilgenkamp, G. Koster, X. H. Verbeek, S. Smit, M. S. Golden, H. A. Dürr, and A. Sakdinawat, *Balanced detection in femtosecond x-ray absorption spectroscopy to reach the ultimate sensitivity limit* (2020), arXiv:2006.13968.
- [46] L. L. Guyader, A. Eschenlohr, M. Beye, W. Schlotter, F. Döring, C. Carinan, D. Hickin, N. Agarwal, C. Boeglin, U. Bovensiepen, J. Buck, R. Carley, A. Castoldi, A. D’Elia, J.-T. Delitz, W. Ehsan, R. Engel, F. Erdinger, H. Fangohr, P. Fischer, C. Fiorini, A. Föhlisch, L. Gelisio, M. Gensch, N. Gerasimova, R. Gort, K. Hansen, S. Hauf, M. Izquierdo, E. Jal, E. Kamil, S. Karabekyan, T. Kluyver, T. Laarmann, T. Lojewski, D. Lomidze, S. Maffessanti, T. Mamyrbayev, A. Marcelli, L. Mercadier, G. Mercurio, P. S. Miedema, K. Ollefs, K. Rossnagel, B. Rösner, N. Rothenbach, A. Samartsev, J. Schlappa, K. Setoodehnia, G. S. Chiuzebaian, L. Spieker, C. Stamm, F. Stellato, S. Techert, M. Teichmann, M. Turcato, B. Van Kuiken, H. Wende, A. Yaroslavtsev, J. Zhu, S. Molodtsov, C. David, M. Porro, and A. Scherz, *Photon shot-noise limited transient absorption soft x-ray spectroscopy at the european xfel* (2022), arXiv:2211.0426.
- [47] P. Denes, D. Doering, H. A. Padmore, J.-P. Walder, and J. Weizeorick, A fast, direct x-ray detection charge-coupled device, *Review of Scientific Instruments* **80**, 083302 (2009).
- [48] F. Januschek, I. Kláčková, N. Andresen, P. Denes, S. Hauf, J. Joseph, M. Kuster, and C. Tindall, Performance of the LBNL FastCCD for the European XFEL, in *2016 IEEE Nuclear Science Symposium, Medical Imaging Conference and Room-Temperature Semiconductor Detector Workshop (NSS/MIC/RTSD)* (2016) pp. 1–3.
- [49] I. Kláčková, G. Blaj, P. Denes, A. Dragone, S. Göde, S. Hauf, F. Januschek, J. Joseph, and M. Kuster, Characterization of the ePix100a and the FastCCD semiconductor detectors for the european XFEL, *Journal of Instrumentation* **14** (01), C01008.
- [50] E. Saldin, E. Schneidmiller, and M. Yurkov, Statistical properties of the radiation from VUV FEL at DESY operating at 30 nm wavelength in the femtosecond regime, *Nuclear Instruments and Methods in Physics Research Section A: Accelerators, Spectrometers, Detectors and Associated Equipment* **562**, 472 (2006).
- [51] K. Hatada and A. Di Cicco, Modeling saturable absorption for ultra short x-ray pulses, *Journal of Electron Spectroscopy and Related Phenomena* **196**, 177 (2014).
- [52] S. Anisimov, B. L. Kapeliovich, and T. L. Perel’man, Electron emission from metal surfaces exposed to ultrashort laser pulses, *Sov. Phys. JETP* **39**, 375 (1973).
- [53] J. Chen, D. Tzou, and J. Beraun, A semiclassical two-temperature model for ultrafast laser heating, *International Journal of Heat and Mass Transfer* **49**, 307 (2006).
- [54] N. Hartley, J. Grenzer, W. Lu, L. Huang, Y. Inubushi, N. Kamimura, K. Katagiri, R. Kodama, A. Kon, V. Lipp, M. Makita, T. Matsuoka, N. Medvedev, S. Nakajima, N. Ozaki, T. Pikuz, A. Rode, K. Rohatsch, D. Sagae, A. Schuster, K. Tono, J. Vorberger, T. Yabuuchi, and D. Kraus, Ultrafast anisotropic disordering in graphite driven by intense hard X-ray pulses, *High Energy Density Physics* **32**, 63 (2019).
- [55] B. Y. Mueller and B. Rethfeld, Relaxation dynamics in laser-excited metals under nonequilibrium conditions, *Phys. Rev. B* **87**, 035139 (2013).
- [56] H.-T. Chang, A. Guggenmos, S. K. Cushing, Y. Cui, N. U. Din, S. R. Acharya, I. J. Porter, U. Kleineberg, V. Turkowski, T. S. Rahman, D. M. Neumark, and S. R. Leone, Electron thermalization and relaxation in laser-heated nickel by few-femtosecond core-level transient absorption spectroscopy, *Phys. Rev. B* **103**, 064305 (2021).
- [57] C. Powell and A. Jablonski, *NIST electron inelastic-mean-free-path database 71, version 1.1* (2000).



- [58] A. Jain, S. P. Ong, G. Hautier, W. Chen, W. D. Richards, S. Dacek, S. Cholia, D. Gunter, D. Skinner, G. Ceder, and K. a. Persson, The Materials Project: A materials genome approach to accelerating materials innovation, *APL Materials* **1**, 011002 (2013).
- [59] K. Persson, [Materials data on Ni \(sg:225\) by materials project](#) (2016).
- [60] E. Bévilion, J. P. Colombier, V. Recoules, and R. Stoian, Free-electron properties of metals under ultrafast laser-induced electron-phonon nonequilibrium: A first-principles study, *Phys. Rev. B* **89**, 115117 (2014).
- [61] Z. Lin, L. V. Zhigilei, and V. Celli, Electron-phonon coupling and electron heat capacity of metals under conditions of strong electron-phonon nonequilibrium, *Phys. Rev. B* **77**, 075133 (2008).
- [62] Z. Lin and L. V. Zhigilei, Temperature dependences of the electron-phonon coupling, electron heat capacity and thermal conductivity in Ni under femtosecond laser irradiation, *Applied Surface Science* **253**, 6295 (2007).
- [63] T. Lojewski, M. F. Elhanoty, L. L. Guyader, O. Grånäs, N. Agarwal, C. Boeglin, R. Carley, A. Castoldi, C. David, C. Deiter, F. Döring, R. Y. Engel, F. Erdinger, H. Fangohr, C. Fiorini, P. Fischer, N. Gerasimova, R. Gort, F. de Groot, K. Hansen, S. Hauf, D. Hickin, M. Izquierdo, B. E. Van Kuiken, Y. Kvashnin, C.-H. Lambert, D. Lomidze, S. Maffessanti, L. Mercadier, G. Mercurio, P. S. Miedema, K. Ollefs, M. Pace, M. Porro, J. Rezvani, B. Rösner, N. Rothenbach, A. Samartsev, A. Scherz, J. Schlappa, C. Stamm, M. Teichmann, P. Thunstrom, M. Turcato, A. Yaroslavtsev, J. Zhu, M. Beye, H. Wende, U. Bovensiepen, O. Eriksson, and A. Eschenlohr, [The interplay of local electron correlations and ultrafast spin dynamics in fcc Ni](#) (2022), [arXiv:2210.13162](#).
- [64] C. Stamm, T. Kachel, N. Pontius, R. Mitzner, T. Quast, K. Holldack, S. Khan, C. Lupulescu, E. F. Aziz, M. Wietstruk, H. A. Dürr, and W. Eberhardt, Femtosecond modification of electron localization and transfer of angular momentum in nickel, *Nature materials* **6**, 740 (2007).
- [65] H. A. Dürr, C. Stamm, T. Kachel, N. Pontius, R. Mitzner, T. Quast, K. Holldack, S. Khan, C. Lupulescu, E. F. Aziz, M. Wietstruk, and W. Eberhardt, Ultrafast electron and spin dynamics in nickel probed with femtosecond x-ray pulses, *IEEE Transactions on Magnetics* **44**, 1957 (2008).

# Supplementary Information for: Electron Population Dynamics Dominate Non-linearities in X-ray Absorption Near-Edge Spectra from Focused FEL Pulses

## DATA ACQUISITION

The experimental X-ray absorption spectra presented here were collected in the scope of a community proposal as the first user-beamtime at the SCS instrument. The intensities of the two beams generated by the beam-splitting zone plate were recorded using a FastCCD detector [1] with  $1920 \times 960$  pixels of  $30 \times 30 \mu\text{m}^2$ . The intensities of both beams were integrated over a Region Of Interest (ROI) corresponding to  $350 \times 350$  pixels each to retrieve the signal and reference intensities for each FEL shot. The high beam divergence due to the zone plate focusing distributed the signal on a 4 mm wide square on the detector 1 m downstream of the sample, thus greatly decreasing the fluence incident per detector area in order to avoid detector saturation. The gas-attenuator was filled with varying low pressure of nitrogen gas to regulate the transmission through the beamline to the required fluence. We refer to low-intensity spectra if the fluence was consistently below the sample damage threshold and the full measurement could be recorded on a single spot, without scanning the sample.

For measuring high-intensity spectra, the fluence often exceeded the material damage threshold, creating shot craters and sometimes causing larger fractures in the support membrane. For measurements at these fluences, the sample holder was scanned at a speed of  $0.5 \text{ mm s}^{-1}$ . Therefore, only about 50% of all FEL shots were transmitted through the windows; in the other cases, one or both beams were blocked or clipped by the frame. The membranes were arranged on the frame in a periodic pattern of two rows of sample and two rows of reference membranes with a distance of 1 mm between rows. This ensured that the two FEL foci always impinged on one row of sample and one reference membranes; a third row was unused in between. Therefore, every time the currently scanned rows were incremented, the upper beam would switch from probing reference membranes to probing sample membranes or vice versa, while the opposite holds for the lower beam. To prevent detector saturation, an additional aluminum filter of about  $13 \mu\text{m}$  thickness was installed in front of the detector during these measurements.

## DETECTOR CALIBRATION

The temperature of the FastCCD rose consistently during operation and required cool-down periods in between measurements, leading to the temperature varying between  $-27^\circ\text{C}$  and  $-5^\circ\text{C}$  not only over time during the

measurement, but also spatially over the detector area. The detector dark signal, as well as the gain coefficients for the three gain settings between which the detector pixels switch automatically, depend on the detector temperature. This made it necessary to reconstruct a temperature-dependent gain calibration. The three temperature-dependent background levels were drawn from dark images collected at various temperatures for each gain setting; the gain coefficients for each setting were drawn from a statistical analysis of the observed gain switching thresholds, such that the calibrated histogram of pixel intensities becomes continuous over all three gain levels. While the calibration accounts for the temperature measured using a temperature sensor on the detector, spatial variations over the detector area remain. The primary effect of this temperature variation was a varying background signal, following a spatial exponential distribution between the detector center and rim, with a higher baseline near the detector center. To account for this, an estimated background signal was derived from the measurements themselves: For a running average of 100 images, the illuminated area was cut out and interpolated using fits to the background level in the non-illuminated area. This additional background variation was then integrated into the gain calibration described above. Furthermore, a mask of hot and dark pixels with irregular behavior was generated from separate measurements and the respective pixels were excluded from the analysis. Despite these corrections, the detector inhomogeneities constitute a significant part of measurement uncertainty in the presented spectra. In particular, the uneven warming of the two detector halves on which the upper and lower beam respectively impinged has the potential of introducing systematic uncertainties. Thus, the shot-sorting algorithm described below was applied separately for all rows where the sample was in the upper beam and the reference in the lower and then to all rows where the orientation was reversed. Fortunately, differences between the temperature of both detector hemispheres affect the two equally sized groups of data (sample up and sample down) with equal and opposite magnitude. Therefore, possible systematic deviations are eliminated in the average over both groups and instead contribute to the statistical uncertainty which is represented in the error shown in Figure 2 of the manuscript.

## EVENT CLASSIFICATION

Furthermore, whenever the sample or reference membrane was torn due to a particularly intense shot, sub-

sequent shots sometimes impinged on the torn rim of the sample, possibly at an angle to the membrane surface, or did not hit any sample material at all. Shots affected in this way were not always trivial to identify from any single measurement parameter, which lead to the following procedure to identify and exclude faulty FEL shots: First, the detector image in the ROI around one beam was compared to an extended ROI around the other beam using a normalized two-dimensional cross-correlation algorithm. For this, the images were first smoothed by convolution with a Gaussian kernel to remove the influence of the rough surface structure of the aluminum filter before applying the cross-correlation function, both algorithms implemented in the scikit-image [2] package. This procedure yields a correlation coefficient and a displacement vector. The correlation coefficient was used as an indicator that both beams were transmitted through a window without significant differences in the wavefront.

Since data-acquisition of the motor encoder for the position transverse to the scanning direction was dysfunctional, the real path of the beam over the sample frame was reconstructed by combining knowledge of the beam position along the scanning direction and the manual notes in the laboratory book with the correlation coefficients between both beams on the detector. In the later analysis of the damaged samples, this allowed associating specific shot craters scrutinized with SEM-microscopy to specific FEL shots.

From the FEL shots which hit sample windows according to this reconstruction, outliers were dropped if either the correlation coefficient dropped below 85 % or the displacement vector deviated by a significant margin (manually calibrated for each measurement setting) from the expected beam-splitting. Likewise, extreme outliers in the ratio of reference to sample intensity were also dropped at this stage. These criteria proved to be largely redundant as they mostly agree with each other on which events to exclude. Using all of these criteria, events where either or both beams are blocked or clipped can be excluded reliably. In Figure 1, the thus excluded points are shown in gray. Each dot represents one FEL shot; its y-position is the logarithmic ratio between sample and reference intensity; the x-position is the photon energy setting of the monochromator, while the gray-scale encodes the Pearson correlation coefficient  $C_{\text{corr}}$  of the two regions of interest.

From the distribution of the remaining events, shown in color, it is obvious that further classification is needed. This is because shots onto a damaged or missing membrane can produce spots with good correlation and the expected displacement vector. These can only be distinguished by the fact that the apparent optical density deviates unreasonably from the expected value at the given photon energy. However, this transmission ratio is also the quantity of interest for the final spectrum. To disen-

tangle events affected by prior sample damage from true measurements, an iterative approach using a Bayesian Gaussian mixture model was utilized: To start, an initial guess for a spectrum is computed using the events that passed filter conditions described above and shown as a green line in Figure 1. Then, for each FEL shot, the deviation of the logarithmic ratio between sample and reference intensity from the initially guessed spectrum is computed. This allows for generating a histogram of these absorbance deviations from the initial guess. Assuming a good guess of the initial spectrum, one may expect that the “good” FEL shots are normally distributed around zero deviation, while shots affected by various sources of uncertainty are distributed with some other distribution, dependent on the type of uncertainty. Thus, the histogram is fitted with four Gaussian distributions which are used as prior probability distributions, the first of which corresponds to “good” FEL shots. Then, the posterior probability of belonging to the category of “good” shots is computed for each FEL shot. These posterior probabilities are used as statistical weights to compute an improved guess of the measured spectrum. This improved guess was convoluted with a Gaussian kernel to prevent over-fitting before using it as a new initial guess for the Gaussian mixture model. The spectrum is considered converged when the average change per iteration anywhere in the spectrum is less than  $5\mu\text{OD}$ . This procedure converges (if at all) within a few (between 3 and 20) iterations to a solution that is robust even against a strong variation of the initial guess. In Figure 1, the thus analyzed shots are shown in colors encoding the final posterior probability  $P_{\text{ok}}$ , indicating the estimate of the model about the validity of each shot. The final guess of the average spectrum is shown as an orange line.

This final procedure rejects outliers purely based on their deviation from the expected value, which requires further justification: In this case, the procedure should return valid results under the condition that all valid FEL shots at a certain photon energy measure a transmission value within a single continuous range. The width of the distribution is resulting from a combination of non-linear changes and measurement noise. This condition must be fulfilled in the present case as long as the fluence-dependent transmission curve of the sample is continuous and a continuous range of pulse energies is contained in the data set (which is the case for SASE fluctuations). Apart from this logic, the rejected outliers do not appear systematic, further supporting the applicability of the algorithm.

#### DETERMINATION OF THE EFFECTIVE SPOT SIZE

The zone plate has a size of  $(1\text{ mm})^2$  and combines a focusing Fresnel zone plate, off-axis by 0.55 mm with

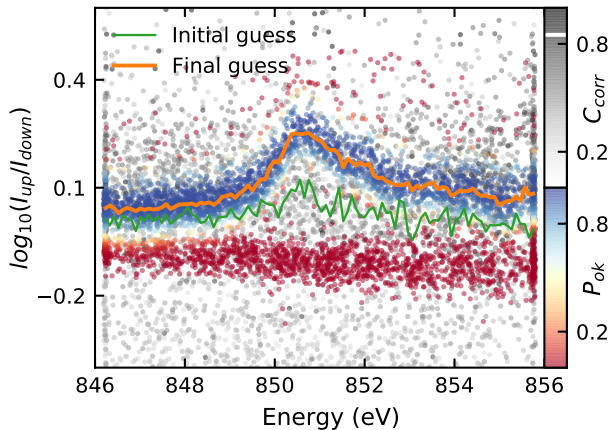


FIG. 1. **Sorting of FEL-shots.** Gray points represent events which were excluded based on rigid criteria, mainly their correlation coefficient  $C_{\text{corr}}$ . Colored points were analyzed using the iterative GMM optimization. The colorbar shows the estimated posterior probability  $P_{0k}$  that a given shot cleanly probed an unperturbed sample. The green and orange solid lines represent the initial and final average spectrum estimated by the GMM, respectively.

250 mm focal length (at 860 eV) with a line grating with 379.4 nm pitch in a single optical element. Details on the zone plate can be found in [3]. While the monochromator was scanned between 846 eV and 856 eV, the effective size of the foci on the sample changed due to the wavelength dependency of the zone plate diffraction. The photon energy-dependent focal size of the zone plate foci was calculated by ray optics calculations based on the beamline settings [4]. Uncertainties in the exact beam path parameters along the beamline were accounted for by matching the ray optics calculations to effective spot size estimates derived from analyzing the shot craters on the used samples using a simplified form of the procedure laid out in [5, 6]. Since a full intensity profile could not be measured from the shot craters, the concept of the effective area of the focal size is used. This area connects the peak fluence  $F_0$  with the overall pulse energy  $E_{\text{pulse}}$ , i.e.

$$A_{\text{eff}} = \frac{E_{\text{pulse}}}{F_0}, \quad (1)$$

and it can be defined for an arbitrary spot profile.

To characterize the effective focal size, the reference membranes were analyzed using scanning electron microscopy (SEM). Figure 2 shows two SEM images: one overview image of an entire membrane one example of a high-resolution image of a single imprint. Such high-resolution images were taken of 85 selected spots which were associated with the corresponding FEL photon diagnostics data by matching the reconstructed movement of the sample stage to the pattern of imprints on the sample. The reference membranes were chosen for the

imprint analysis since their X-ray absorbance can be considered constant for the scanned photon energies.

Since the zone plate is a diffractive element, its properties such as focal length are energy-dependent. Furthermore, the fluence-dependent spectra presented in this paper are combined from measurements at two distinct object distances of 250.84 mm and 252.14 mm.

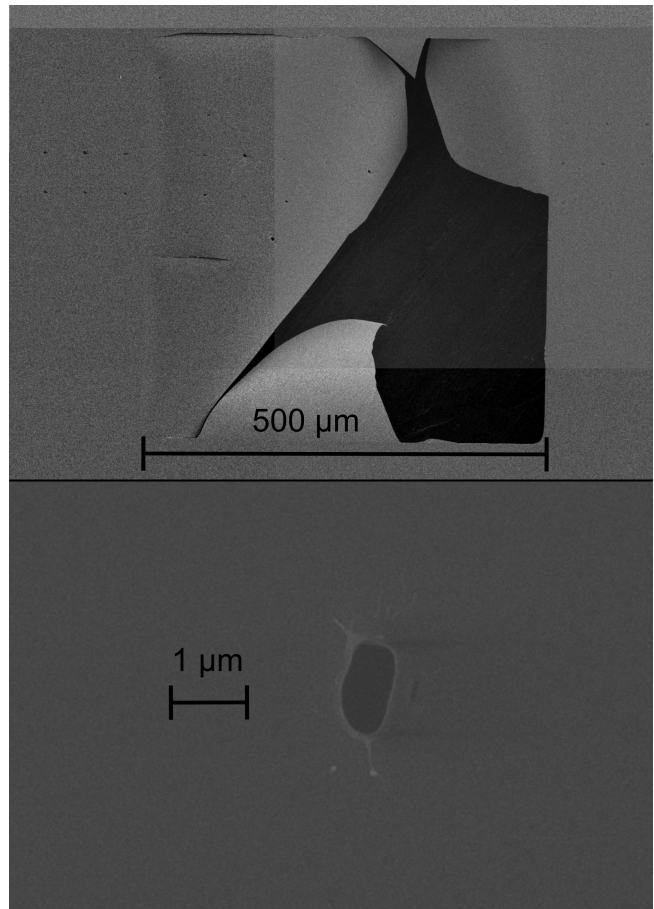


FIG. 2. **SEM images of the used samples** The top image shows a stitched overview image of a nickel film window. One can see rows of FEL imprints as well as the tearing of the membrane. The bottom image shows a single FEL imprint in a SiN reference membrane.

Thus, the SEM images were grouped into six groups (see table I) by focal length and photon energy of the associated shot, and the total damaged or ablated surface area was determined for each shot. For each group, the minimum FEL pulse energy at which damage is observed on the reference membranes was determined by a Liu's plot [7] as shown in Figure 3: The ablated area was plotted over the logarithm of the shot energy and a linear fit was applied to the shots with less than  $1 \mu\text{m}^2$  ablated area to determine the pulse energy damage threshold. Following the concept outlined in [5], the pulse energy of all shots was then normalized using this damage threshold to derive the normalized fluence level  $f(S)$  as a func-

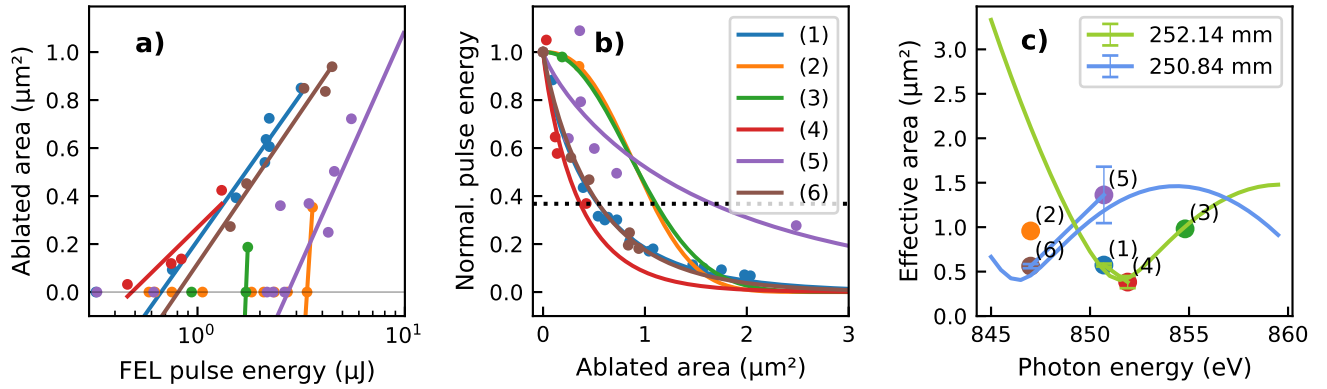


FIG. 3. **Spot size characterization.** a) Liu’s plot to determine the pulse energy damage thresholds. b) Normalized pulse energy plot to determine the effective area. The legend differentiates the spot groups corresponding to table I with colors valid for all three panels. c) Area of FEL foci, comparing the effective area measurements (dots and error bars) to the ray tracing results (line plots) for two focal distances. For groups (2) and (3) no error estimate could be calculated (see text).

Group	Object distance (mm)	Photon energy (eV)	Pulse energy threshold ( $\mu\text{J}$ )	Effective area ( $\mu\text{m}^2$ )
1	252.14	850.7	0.308	0.584
2	252.14	847.0	3.374	0.957
3	252.14	854.8	1.712	0.981
4	252.14	851.9	0.482	0.383
5	250.84	850.7	2.733	1.618
6	250.84	847.0	0.807	0.567

TABLE I. **Results of the spot size characterization.** The object distance refers to the distance between sample and zone plate. Pulse energies are shown as measured at the XGM without accounting for the efficiency of the zone plate (about 9%) and the transmission of the beamline KB-mirrors (about 80%). The effective area of groups 2 and 3 is under-determined (see text).

tion of the ablated area  $S$ . If the spot size were Gaussian, the function  $f(S)$  should be a simple negative exponential, and the effective area would correspond to the value of  $S$  where  $f(S)$  equals  $1/e$ , which is indicated in Figure 3 b) as a horizontal dotted line. For the given non-Gaussian case, the function  $f(S)$  was fitted with a modified exponential  $f(S) = e^{-aS^b}$ , yielding for each group of shots fit parameters  $a$  and  $b$  and their uncertainties  $\sigma_a$  and  $\sigma_b$ . The effective area is then calculated as the integral of  $f(S)$ . For the estimate of the uncertainty shown as error bars of Figure 3 c), the integral was also evaluated for  $a + \sigma_a$  and  $b + \sigma_b$  as well as  $a - \sigma_a$  and  $b - \sigma_b$ . Groups (2) and (3) each contained only a single FEL shot with visible damage. While this does allow for an estimate of the damage threshold (compare Figure 3 a)), the function  $f(S)$  shown in b) is barely determined by fitting only to the normalization point and a single further point. Thus, no mathematical uncertainty estimate can be given and resulting points (2) and (3) shown without error bars in Figure 3 c) should be considered as tentative estimates. The ray optics calculation tracks the beams in the vertical and horizontal planes. The focus area was calculated from the ray optics calculations assuming an elliptical beam shape. It revealed a slightly astigmatic focus on the sample, due to the beamline optics using separate hori-

zontal and vertical focusing, thus illuminating the zone plate with slightly non-uniform beam divergence. The separate location of horizontal and vertical foci leads to the two minima visible in Figure 3. Based on the measurements, a minimal beam-waist radius of 80 nm was imposed on the ray tracing calculations, accounting for imperfections in beam quality and optics.

The fluences for the high-fluence spectra shown in this paper are calculated based on the pulse energy measured by the XGM behind the monochromator, multiplied with the efficiency of the focusing optics (80%) [8] and zone plate (9%) and divided by the effective area derived with the presented ray optics calculations. Since the XGM was calibrated for high pulse energies, the fluences for the low-fluence spectra are based on the reference intensities measured on the CCD and calibrated to be consistent with the reference intensities measured for the high-fluence data, accounting for the calculated transmission of the aluminum filter.

[1] F. Januschek, I. Klačková, N. Andresen, P. Denes, S. Hauf, J. Joseph, M. Kuster, and C. Tindall, Performance of the LBNL FastCCD for the European XFEL, in [2016](#)



- IEEE Nuclear Science Symposium, Medical Imaging Conference and Room-Temperature Semiconductor Detector Workshop (NSS/MIC/RTSD)* (2016) pp. 1–3.
- [2] S. Van der Walt, J. L. Schönberger, J. Nunez-Iglesias, F. Boulogne, J. D. Warner, N. Yager, E. Gouillart, and T. Yu, scikit-image: image processing in python, *PeerJ* **2**, e453 (2014).
- [3] F. Döring, B. Rösner, M. Langer, A. Kubec, A. Kleibert, J. Raabe, C. A. F. Vaz, M. Lebugle, and C. David, Multifocus off-axis zone plates for x-ray free-electron laser experiments, *Optica* **7**, 1007 (2020).
- [4] L. L. Guyader, Boz calculator, <https://rtd.xfel.eu/docs/bozcalc/en/latest/> (2022).
- [5] J. Chalupský, J. Krzywinski, L. Juha, V. Hájková, J. Cihelka, T. Burian, L. Vyšín, J. Gaudin, A. Gleeson, M. Jurek, A. R. Khorsand, D. Klinger, H. Wabnitz, R. Sobierajski, M. Störmer, K. Tiedtke, and S. Toleikis, Spot size characterization of focused non-gaussian x-ray laser beams, *Opt. Express* **18**, 27836 (2010).
- [6] R. Sobierajski, M. Jurek, J. Chalupský, J. Krzywinski, T. Burian, S. D. Farahani, V. Hájková, M. Harmand, L. Juha, D. Klinger, R. A. Loch, C. Ozkan, J. B. Peřka, K. Sokolowski-Tinten, H. Sinn, S. Toleikis, K. Tiedtke, T. Tschentscher, H. Wabnitz, and J. Gaudin, Experimental set-up and procedures for the investigation of XUV free electron laser interactions with solids, *Journal of Instrumentation* **8** (02), P02010.
- [7] J. M. Liu, Simple technique for measurements of pulsed gaussian-beam spot sizes, *Optics letters* **7**, 196 (1982).
- [8] G. Mercurio, J. Chalupský, I.-T. Nistea, M. Schneider, V. Hájková, N. Gerasimova, R. Carley, M. Cascella, L. L. Guyader, L. Mercadier, J. Schlappa, K. Setoodehnia, M. Teichmann, A. Yaroslavl'tsev, T. Burian, V. Vozda, L. Vyšín, J. Wild, D. Hickin, A. Silenzi, M. Stupar, J. T. Delitz, C. Broers, A. Reich, B. Pfau, S. Eisebitt, D. L. Civita, H. Sinn, M. Vannoni, S. G. Alcock, L. Juha, and A. Scherz, Real-time spatial characterization of micrometer-sized x-ray free-electron laser beams focused by bendable mirrors, *Opt. Express* **30**, 20980 (2022).